

ARTICLE

OPEN



Dynamic substrate reactions during room temperature heavy ion irradiation of CoCrCuFeNi high entropy alloy thin films

Timothy G. Lach¹✉, Chinthaka M. Silva^{1,2}, Yufan Zhou¹, Walker L. Boldman³, Philip D. Rack¹, William J. Weber¹ and Yanwen Zhang^{1,3}

High entropy alloys (HEAs) are promising materials for various applications including nuclear reactor environments. Thus, understanding their behavior under irradiation and exposure to different environments is important. Here, two sets of near-equiatomic CoCrCuFeNi thin films grown on either SiO₂/Si or Si substrates were irradiated at room temperature with 11.5 MeV Au ions, providing similar behavior to exposure to inert versus corrosion environments. The film grown on SiO₂ had relatively minimal change up to peak damage levels above 500 dpa, while the film grown on Si began intermixing at the substrate–film interface at peak doses of 0.1 dpa before transforming into a multi-silicide film at higher doses, all at room temperature with minimal thermal diffusion. The primary mechanism is radiation-enhanced diffusion via the inverse Kirkendall and solute drag effects. The results highlight how composition and environmental exposure affect the stability of HEAs under radiation and give insights into controlling these behaviors.

npj Materials Degradation (2022)6:60; <https://doi.org/10.1038/s41529-022-00260-2>

INTRODUCTION

Alloys in reactor environments require phase stability to maintain physical and mechanical properties and component performance. Exposure to multiple concurrent extremes found in reactor environments, such as radiation, high temperature, mechanical stress, and/or environmental exposure, can lead to synergistic effects on materials that are not observed if exposed to these extremes individually or sequentially¹. Radiation resistance can be imparted by having a nanocrystalline material with a high density of interface sinks². Similarly, radiation resistance can also be imparted by reducing defect generation and defect mobility, such as using chemical disorder, low thermal conductivity, and large lattice distortions found in high entropy alloys (HEAs)^{3–10}. However, that radiation resistance becomes meaningless if the nano-sized grains or chemically complex alloys lose their stability resulting in excessive grain growth or formation of other phases when exposed to other extremes like high temperatures or corrosive environments. Oxidation rates in high temperature air or steam of HEAs, just like stainless steels, depend on the composition of the alloy and what the phase of the oxide scale that forms^{11–13}.

Similar to oxidation and corrosion, irradiation can have a large impact on the phase stability of these materials. Combining corrosion and irradiation is an area of research that is garnering much interest. However, there is limited knowledge of how simultaneous irradiation and environmental exposure affect phase stability, particularly in HEAs. Studies investigating sequential irradiation followed by corrosion showed either no effect on corrosion rates¹⁴ or an enhancement of the corrosion rate¹⁵. Only recently have there been studies on the synergistic effects of irradiation and corrosion simultaneously, with some showing radiation-enhanced corrosion and others showing radiation-decelerated corrosion^{14,16,17}. In these works, whether corrosion is aided by irradiation was determined to depend on the corrosive medium. Each study, though, attested to the

importance of radiation-enhanced diffusion (RED) as the primary means of radiation enhanced or decelerated corrosion, and thus on defect migration. However, those studies have mainly focused on simple model alloys or conventional alloys and steels. There is a limited mechanistic understanding of how chemical complexity in HEAs may affect the combined radiation-environmental exposure behavior, which have been shown to reduce defect generation and migration under irradiation⁷. Thus, it is important to understand how these alloys either maintain or lose microstructural or phase stability and what type of mitigation mechanisms can be imposed to stop or slow down phase and microstructural evolution under multiple environmental extremes.

Multiple principal element alloys, of which HEAs are a subset, expand alloy design space by increasing compositional complexity to three or more elements—primarily transition metals—of near-equiatomic composition. The chemical complexity and high entropy often stabilize a disordered but simple atomic structure such as face centered cubic (fcc) or body centered cubic (bcc). The bcc phase HEAs are dominated by refractory metals like W, Mo, Nb, and Ta, while the fcc phase HEAs are dominated by the period 4 metals, like Co, Cr, Fe, Ni, Cu, and Mn. These alloys have been extensively studied in recent years to determine their irradiation response^{18–20} or their oxidation or corrosion response^{11,21–25}, which depending on composition can exceed that of traditional steels and high temperature alloys. The focus in this work is on the fcc HEA alloys consisting of equal amounts of Co, Cr, Cu, Fe, and Ni. They have been shown to have excellent phase stability under irradiation or thermal annealing and retain a nanocrystalline grain structure⁶. However, the synergistic effects of combined irradiation, high temperature, and/or environmental exposure on these alloys are unknown.

Here the synergistic effects of heavy ion radiation and environmental exposure are characterized on fcc nanocrystalline

¹Materials Science and Technology Division, Oak Ridge National Laboratory, Oak Ridge, TN 37830, USA. ²Materials Science Division, Lawrence Livermore National Laboratory, Livermore, CA 94550, USA. ³Department of Materials Science and Engineering, University of Tennessee, Knoxville, TN 37996, USA. ✉email: lachtg@ornl.gov

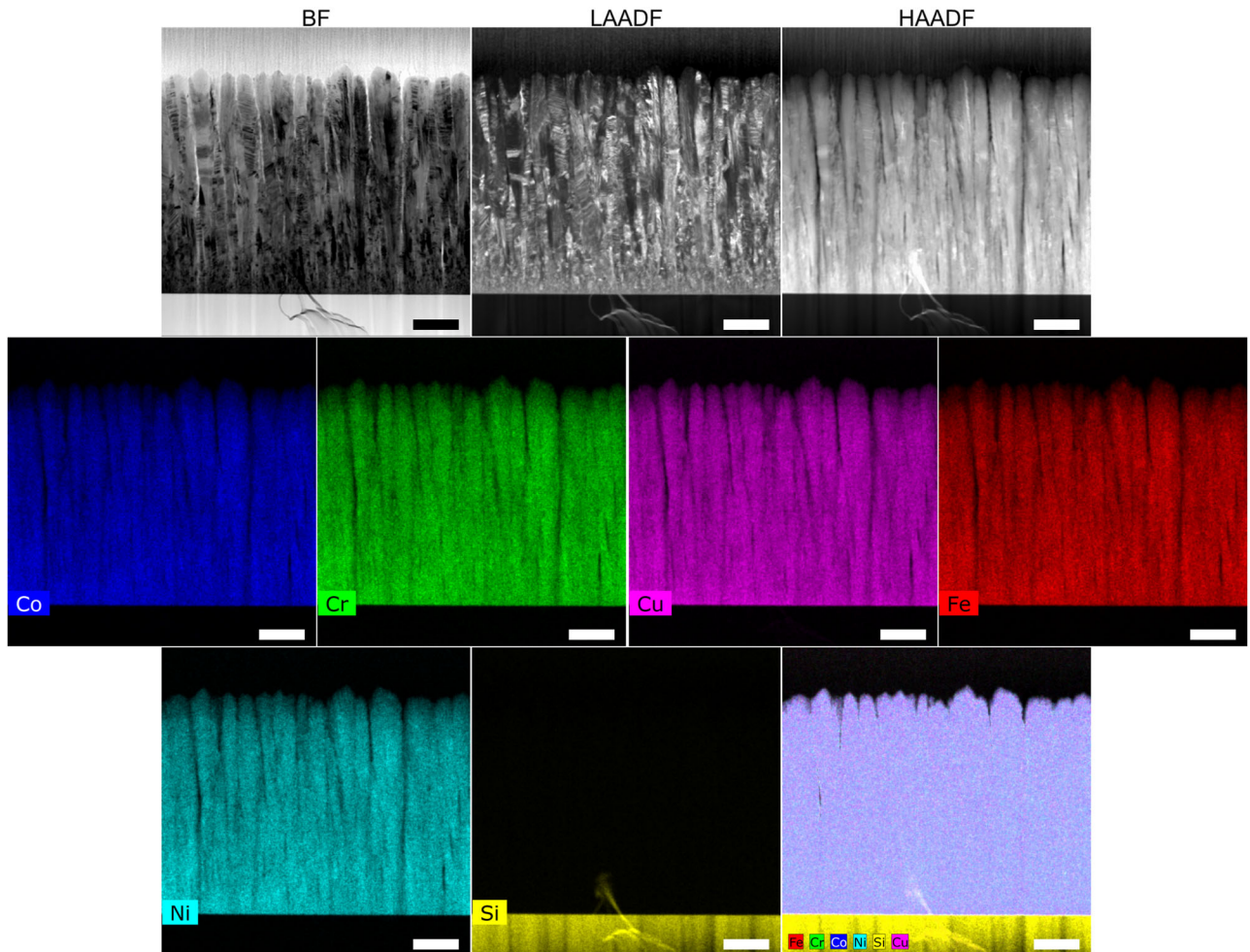


Fig. 1 As-grown HEA film on Si is in solid-solution. STEM-BF, LAADF, and HAADF images and EDS maps of the as-grown CoCrCuFeNi film on a Si substrate. The scale bar length in all images is 200 nm.

HEA thin films grown on substrates with varying levels of reactivity: Si and SiO_2 . While not traditionally thought of as being an ‘environment’ nor as a corrosive medium such as air, steam, or water exposure, the substrate of a film or the solid interface between two joined materials can likewise serve as a similar surrogate for investigation due to differences in chemical potential and reaction kinetics. Just as the interface between a steel and a molten salt¹⁷ or a liquid Pb–Bi eutectic phase¹⁶ have different corrosion behavior under irradiation, the solid interface between an HEA film and the substrate can have drastically different phase stability behavior depending on chemical elements in the substrate material. Beyond nuclear energy applications, the interface between HEAs and Si is important for diffusion barrier coatings for Cu interconnects in nanoscale transistors^{26–28}. To further improve the processing ability of microelectronics, Cu has largely replaced Al as the interconnect material due to its higher electrical conductivity; however, it preferentially forms Cu-silicides if an effective diffusion barrier is not present²⁹. While not the primary concern here, this work will provide insights for using HEAs as diffusion barrier coatings on Si as well. This work used scanning transmission electron microscopy (STEM) with energy-dispersive x-ray spectroscopy (EDS) combined with x-ray diffraction (XRD) to understand the behavior of CoCrCuFeNi HEA films grown Si or SiO_2 substrates to understand the effects of irradiation on phase stability at the film–substrate interface.

RESULTS

As-grown CoCrCuFeNi films

Thin films of near-equiaxial CoCrCuFeNi were grown on Si substrates with or without an SiO_2 interface layer. Figures 1 and 2 show the cross-section STEM bright field (BF) and annular dark field (ADF) images and energy-dispersive spectroscopy (EDS) elemental maps for each film, respectively. They both are 1 μm -thick films and are chemically homogeneous. Within about 100 nm of the substrate, the grains are small and equiaxed before forming columnar grain structures that make up the rest of the film thickness. The columnar grains are about 50 nm across and are made up of a high density of sub-grains and twins. There is no apparent difference between the films except for the substrate, with the film shown in Fig. 2 having a 100 nm-thick SiO_2 above the Si substrate surface. As will be shown, this difference is significant when the films are subjected to ion irradiation or thermal annealing.

Highest fluence, room temperature irradiation of films on both Si and SiO_2/Si

Room temperature ion irradiation with 11.5 MeV Au ions was conducted at several doses up to a dose of $6.0 \times 10^{16} \text{ cm}^{-2}$. The Stopping and Range of Ions in Matter (SRIM) code with the option of Detailed Calculation with full Damage Cascades was used to estimate average dose in displacements per atom (dpa) in the film

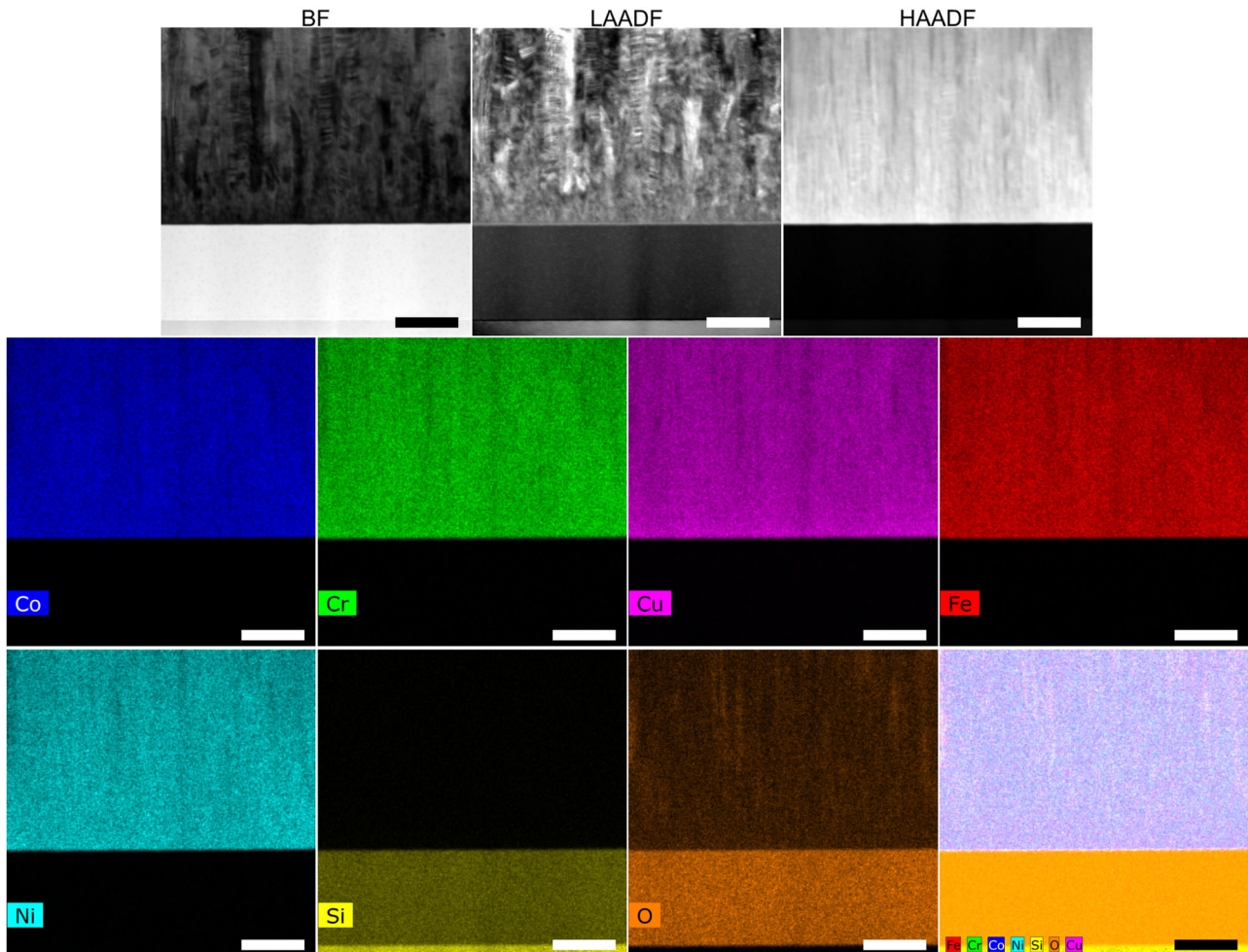


Fig. 2 As-grown HEA film on SiO_2/Si is in solid-solution. STEM-BF, LAADF, and HAADF images and EDS maps of the as-grown CoCrCuFeNi film on a SiO_2 substrate. The scale bar length in all images is 70 nm.

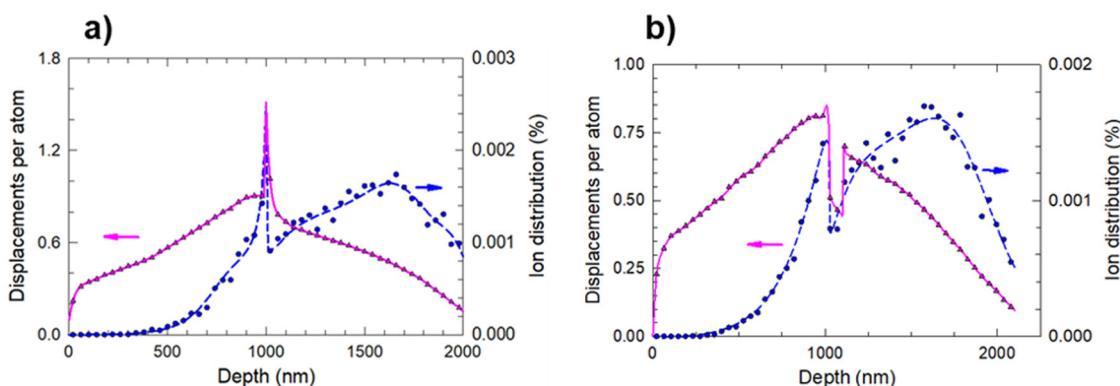


Fig. 3 Calculated damage profile for high energy Au implantation into both sets of films. SRIM predicted dpa profile to an ion fluence of $1 \times 10^{14} \text{ cm}^{-2}$ (left axis) and implanted ion distribution (right axis) for 11.5 MeV Au ions into **a** 1 μm HEA film on Si and **b** 1 μm HEA film on SiO_2/Si .

and implanted ion distribution along an ion trajectory. The density of 8.356 g cm^{-3} was used in the SRIM calculations. The threshold displacement energy of 40 eV was used for the metallic elements, 28 eV for O, and 15 eV for Si. The dpa profile (Fig. 3) based on full-cascade option^{30,31} is the sum of the vacancies from all target elements plus the replacement collisions.

A dose of $6.0 \times 10^{16} \text{ cm}^{-2}$ resulted in an enormous change in the structure and elemental distribution of the film grown on a Si substrate, as shown in the STEM images and EDS maps in Fig. 4. In contrast, only small changes in the film that was grown on a SiO_2/Si substrate display the 'environmental' impact, which is associated with the SiO_2 layer, as shown in Fig. 5. Based on the

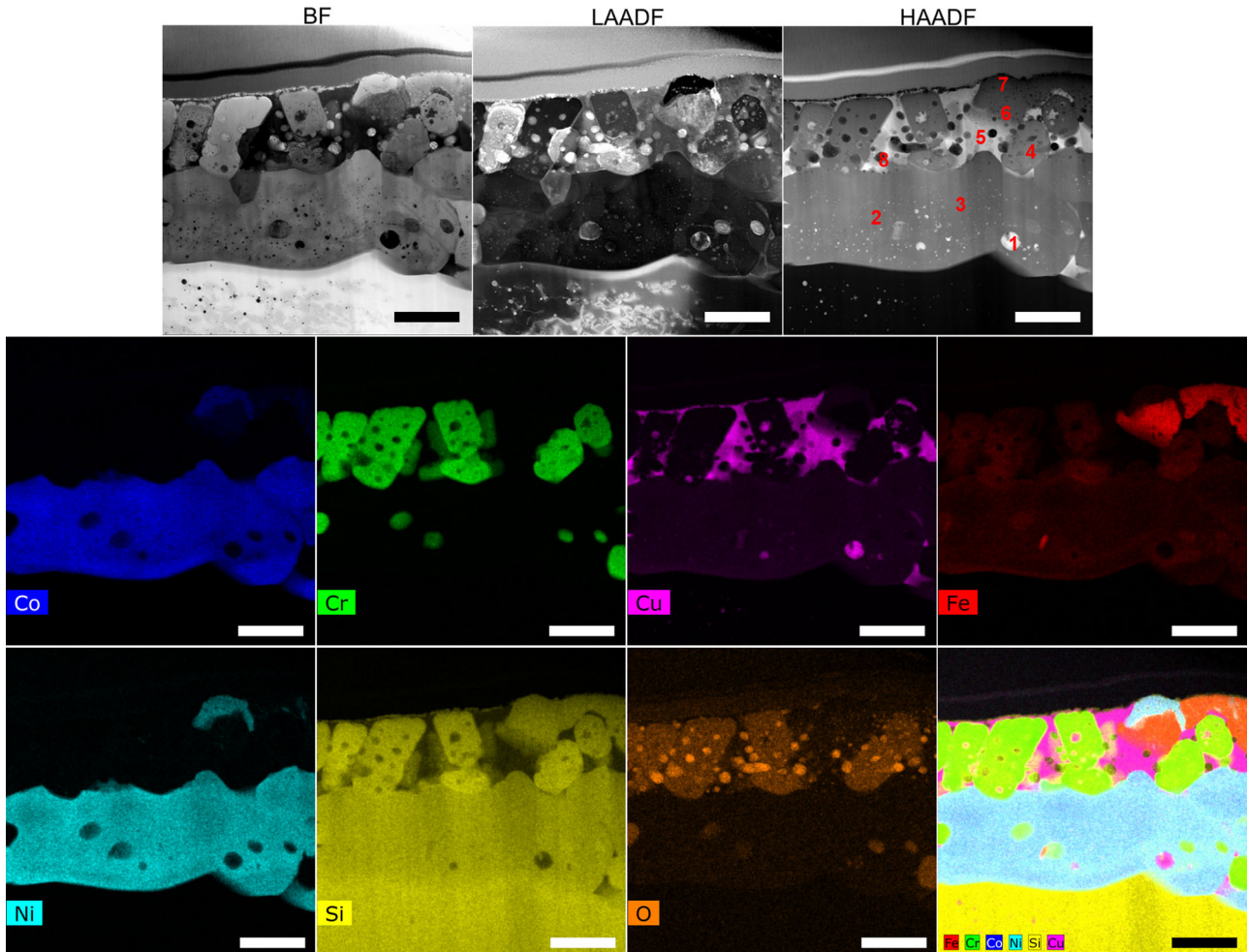


Fig. 4 HEA film grown on Si after high ion irradiation fluence undergoes large-scale structural change. STEM-BF, LAADF, and HAADF images and EDS maps of the CoCrCuFeNi film grown on a Si substrate after room temperature 11.5 MeV Au-ion irradiation to a fluence of $6.0 \times 10^{16} \text{ cm}^{-2}$ (peak of $\sim 507 \text{ dpa}$). The scale bar length in all images is 800 nm.

SRIM evaluation in Fig. 3, the peak damage dose in the film is $\sim 507 \text{ dpa}$ at this fluence. In the film grown on Si, there are many features to point out. The region that contains any of the five elements from the film has a thickness of $2.3 \pm 0.3 \mu\text{m}$, up from the $1 \mu\text{m}$ as-grown film thickness. This region is effectively comprised of two layers: a bottom layer that has large grain size with $>1\text{--}2 \mu\text{m}$ lateral size and a thickness of $\sim 1.1 \pm 0.2 \mu\text{m}$, and a top layer that has lateral grain size of $\sim 500 \pm 100 \text{ nm}$ and a thickness of $1 \pm 0.1 \mu\text{m}$. The bottom layer consists primarily of a (Co,Ni)-rich silicide with particles of Cr-rich silicide and Cu-rich silicide. The top layer consists of large Cu-rich silicide regions along with Cr-rich silicide, (Co,Ni)-rich silicide, and Fe-bearing silicide. Fe appears to be present in all the silicide phases, but there appear to be regions that are primarily Fe-silicide. The composition of several regions using STEM-EDS point analysis using Cliff-Lorimer quantification (spots shown in the STEM-high angle ADF (HAADF) image in Fig. 4) is presented in Table 1. The first three spots are in the bottom layer. Based on composition ratios and in comparison with binary phase diagrams^{32–36}, the bulk of the bottom layer consists of a (Co,Ni)Si₂ phase. The particles in the bottom layer are likely Cu₃Si and CrSi₂. Spots 4–8 are in the top layer. Most of this layer consists of MSi₂ phases, where M = Cr, Fe, and to a lesser extent (Co, Ni). The exception is the Cu-rich regions, which appear to be more Cu-rich than the Cu-rich particles in the bottom layer; these Cu-rich regions may

be Cu₁₅Si₄ when compared to the binary Cu-Si phase diagram³⁴. The oxygen signal may show either the presence of M-oxide phases or are evidence of void space via being an artifact (as these regions are dark in HAADF). The O k- α peak also overlaps with the Cr L- α peak and can be an artifact where Cr is present, and where the Cr signal is weak and O is rich, is real.

On the other hand, the film grown on SiO₂ showed nearly the opposite behavior. After irradiation, the film, as shown in the STEM imaging and EDS maps in Fig. 5 shows only slight changes after very high dose ion irradiation at room temperature. The columnar grain width is still $\sim 50 \text{ nm}$. There are four observable changes that are much smaller in scale compared to the film grown on Si: (1) formation of Cr-rich oxide particles and segregation of Fe near the film surface, (2) segregation of Cr to the columnar grain boundaries, (3) precipitation of small Cu clusters throughout the film, and (4) a roughening of the interface between the film and the SiO₂ substrate layer (see refs. ^{31,37} for a comprehensive evaluation of this sample). The difference in radiation response clearly shows that variation in environmental exposure (i.e., interface with Si or SiO₂) during irradiation can have profound importance on radiation response. The Si clearly interacts with the HEA film where metal elements diffuse into the substrate and/or Si diffuses into the film during irradiation, while the SiO₂ remains relatively inert and acts as an effective barrier between HEA film and Si substrate.

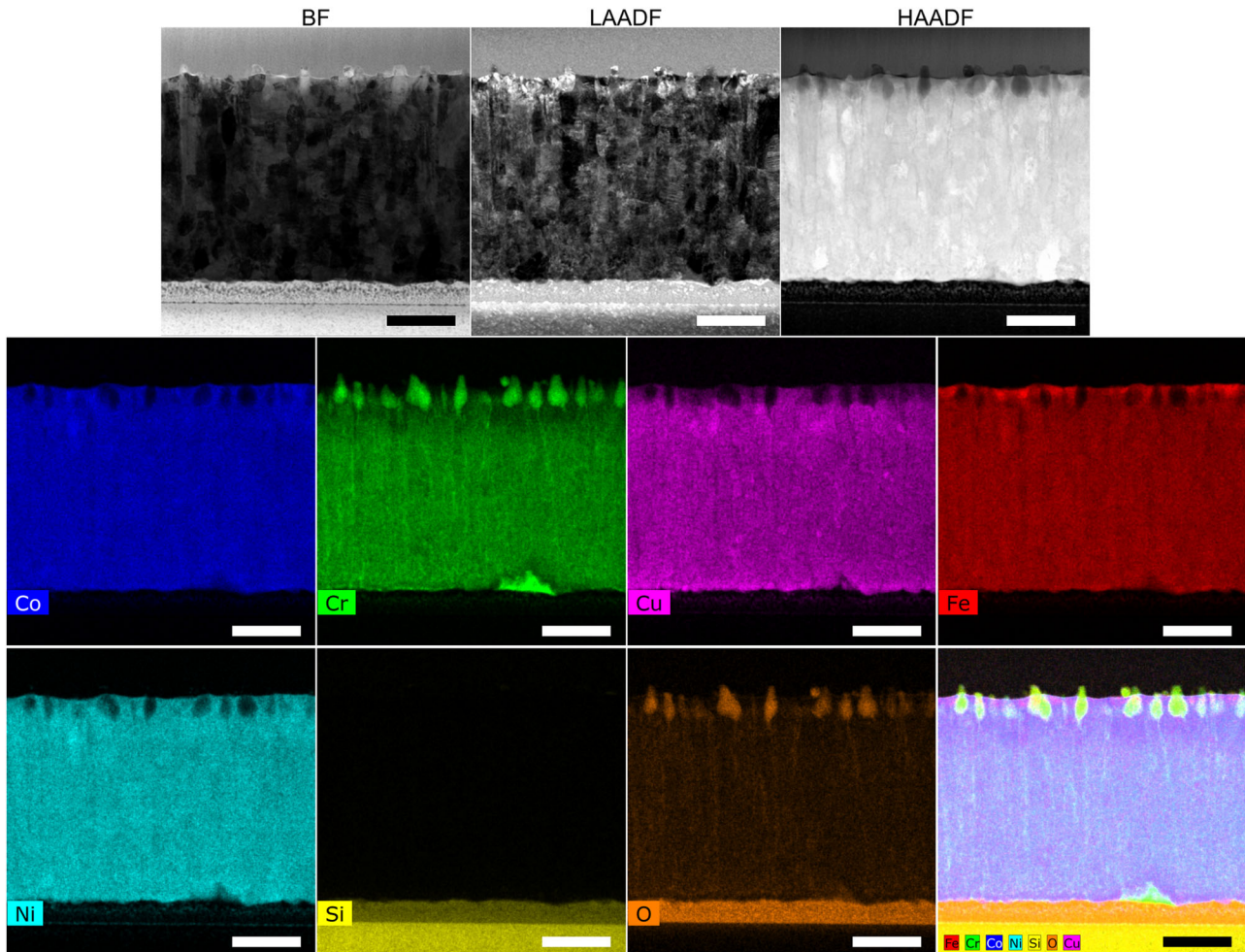


Fig. 5 HEA film grown on SiO_2/Si after high ion irradiation fluence undergoes minimal structural change. STEM-BF, LAADF, and HAADF images and EDS maps of the CoCrCuFeNi film grown on a SiO_2 on Si substrate after room temperature 11.5 MeV Au-ion irradiation to a fluence of $6.0 \times 10^{16} \text{ cm}^{-2}$ (peak of ~ 507 dpa). The scale bar length in all images is 300 nm.

Table 1. Concentration (at%) determined by STEM-EDS and potential structure of the spots denoted in Fig. 4.

Spot	Co	Cr	Cu	Fe	Ni	Si	O	Potential structure
Ref.	18.4	16.2	29.1	16.2	19.6	0.4		HEA
1	2.0	0.1	67.0	0.8	3.0	25.8	1.4	Cu_3Si
2	5.6	16.7	4.6	5.2	5.9	61.4	0.6	CrSi_2
3	16.2	0.1	2.8	3.2	15.4	60.9	1.4	$(\text{Co},\text{Ni})\text{Si}_2$
4	0.1	27.0	4.8	5.5	0.2	60.8	1.6	CrSi_2
5	0.1	0.0	77.7	0.1	0.1	18.4	3.5	$\text{Cu}_{15}\text{Si}_4$
6	3.1	0.4	3.2	25.9	0.6	62.1	4.7	FeSi_2
7	13.5	0.1	3.1	3.8	14.6	61.4	3.6	$(\text{Co},\text{Ni})\text{Si}_2$
8	0.2	9.4	12.8	1.5	0.2	43.3	32.5	unknown

Analysis of low and intermediate dose, room temperature irradiation of film on Si substrate

With the extreme changes after high dose radiation identified on the film grown on Si, the mechanisms for these changes need to be identified. Here, the low and intermediate dose room temperature radiation response is investigated and compared with elevated temperature thermal annealing. At a low fluence of $4.9 \times 10^{13} \text{ cm}^{-2}$ as shown in Supplementary Fig. 1, the CoCrCuFeNi

film on the SiO_2/Si substrate resembles the as-grown film without any noticeable changes; though as will be noted, there is a slight enrichment of Cu, Co, Ni, and Fe at the interface. Based on the SRIM evaluation in Fig. 3, the peak damage dose in the film is only about 0.4 dpa at this fluence. However, as the dose is increased $\sim 2.4\times$ to a fluence of $1.2 \times 10^{14} \text{ cm}^{-2}$ and a peak damage dose in the film of 1.0 dpa, an interaction between the film and Si substrate becomes readily apparent, as is shown in Fig. 6. It appears that Co, Cu, Fe, and Ni have diffused into the Si substrate, while Cr does not. The insertion of those four elements is not uniform as islands with varying concentration have formed, though each region appears to be particularly elevated in its Ni content and slightly lower in its Fe content, based on the point analysis captured in Table 2. There also is a small movement of Si atoms into the film based on the concentration in spot 2 compared to the reference film and farther away from the substrate (spot 1).

As the dose is further increased about $6\times$ to a fluence of $7.1 \times 10^{14} \text{ cm}^{-2}$ and a peak damage in the film of about 6.1 dpa, the interaction between the film and Si substrate intensifies, as there are seven distinctive regions that have formed in a heterogeneous multilayered fashion, as is shown in Fig. 7. The bottom region, region 1, is the pure Si substrate. Above this is a zone of Cu-rich Cu-Si islands of ~ 100 nm in width with large voids within the same plane. Above this, in region 3, is an ~ 20 nm-thick layer of Ni-rich silicide. Region 4 is a thicker ~ 40 nm Si-rich layer enriched in Co, Fe, and Ni. Above this is region 5

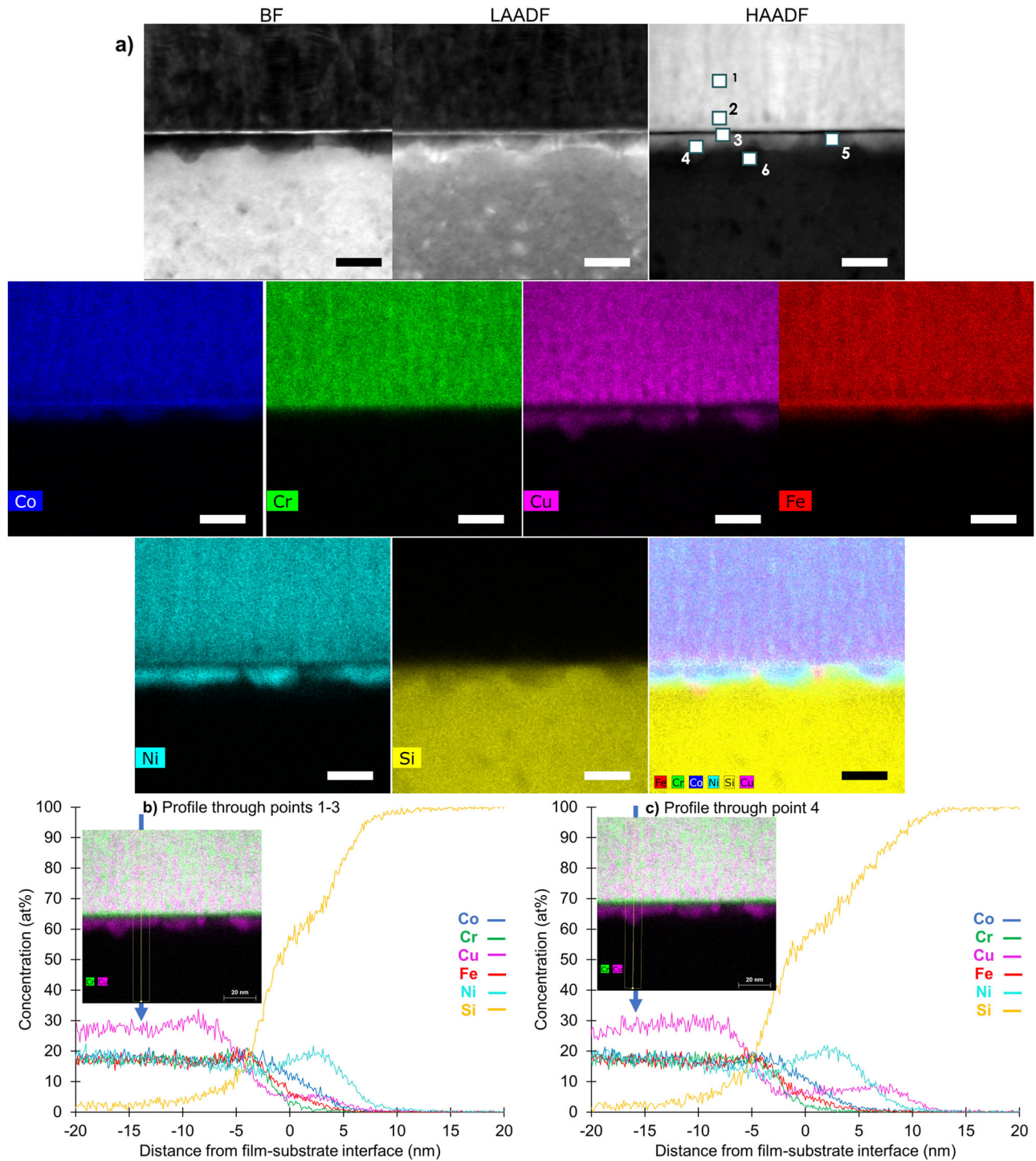


Fig. 6 The interface between the HEA film and Si substrate begins to noticeably evolve after low fluence Au-ion irradiation. **a** STEM-BF, LAADF, and HAADF images and EDS maps of the CoCrCuFeNi film grown on a Si substrate after room temperature 11.5 MeV Au-ion irradiation to a fluence of $1.2 \times 10^{14} \text{ cm}^{-2}$ (peak of $\sim 1.0 \text{ dpa}$); HAADF has spots marked where EDS point analysis was taken—see Table 2. The scale bar length in all images is 20 nm. Concentration profile normal to the interface through **b** points 1–3 and **c** point 4.

which is another Ni-rich layer that also has some Co and Fe, and a small amount of Cr. Region 6 is the Cr-rich layer that has more Cr than Si or the other metals. This layer also has $\sim 50 \text{ nm}$ wide voids that are regularly spaced apart. Lastly, region 7 is the intact HEA film.

Further increasing the fluence by a factor of ~ 5 to $3.8 \times 10^{15} \text{ cm}^{-2}$ and a peak damage in the film of about 32.4 dpa leads to a major change where the original film is no longer intact.

As evidenced in Fig. 8, the film, and the substrate directly beneath it, have been overtaken by large voids that are near $1 \mu\text{m}$ in diameter. Based on the concentration profile, near the sample surface, there is about 300 nm of mostly metallic film, though it is depleted in Cr, Cu, and Ni relative to Co and Fe. A multilayered structure present in Fig. 7 is still somewhat present here, where a thick Ni-rich layer lies below a Co and Fe-rich layer which is below

Table 2. Concentration (at%) determined by STEM-EDS and potential structure of the spots denoted in Fig. 6.

Spot	Co	Cr	Cu	Fe	Ni	Si	Potential structure
Ref.	18.4	16.2	29.1	16.2	19.6	0.4	HEA
1	18.9	16.3	27.2	17.1	19.7	1.0	HEA
2	17.5	17.2	28.6	17.0	16.6	3.0	HEA
3	11.0	3.4	5.3	6.2	18.2	55.8	(Co,Ni)Si
4	3.9	0.7	7.8	2.1	16.8	68.7	(Ni,Cu)Si ₂
5	3.7	1.1	2.5	1.9	9.3	81.5	Si
6	0.3	0.1	0.8	0.2	0.8	97.9	Si

the Cr-rich layer. All three of these layers are Si-enriched, with the bottom two layers comprised of MSi₂, where M = Ni or (Co, Fe), and the top Cr-rich layer having a CrSi composition. Cu atoms have largely depleted from the original film and moved into the Si substrate. The large Cu-rich region in Fig. 8 has a composition that is close to the Cu_{0.83}Si_{0.17} phase. As the radiation dose increases, decomposition of the HEA film leads to the formation of mostly metal silicides.

Further increasing the dose by another factor of ~5 to $2.0 \times 10^{16} \text{ cm}^{-2}$ and a peak damage in the film of 172.6 dpa leads to a major change where the original film is no longer recognizable, as shown in Fig. 9, and resembles the thick layered structure found at the highest dose in Fig. 4. The progression from lower doses is clear. Cu has moved farthest into the Si substrate, followed by Ni and Co. Cr remains near the original film/substrate interface. However, at this point, it appears that recrystallization and grain growth have added to the mix. There is no sense of the original columnar grain structure. The whole film has turned into a multi-phase silicide. The Cu-rich phase at the bottom has the same composition as in Fig. 8, of Cu_{0.83}Si_{0.17}. The rest of the film has turned into various forms of MSi₂, where M is a varying assortment of Co, Cr, Ni, and Fe, with distinct regions that are Cr-rich, Fe-rich, (Cr,Fe)-rich, Ni-rich or (Co,Ni)-rich.

Irradiation-induced phase formation validated by XRD

XRD analysis supports the large-scale formation of silicides, similarly to what was found by STEM and STEM-EDS analysis. In Fig. 10 and Table 3, at fluences of $7.1 \times 10^{14} \text{ ions/cm}^2$ or less, only the fcc phase and Si phase are found, except for some small peaks that are barely above the background and potentially correspond with an oxide phase, M₃O₄. Even though Bragg peaks corresponding to an oxide (M₃O₄) phase were not prominent enough to apply Rietveld refinement to fit the phase, the samples irradiated to $7.1 \times 10^{14} \text{ cm}^{-2}$ indicated the possible presence of the oxide, which is consistent with the STEM-EDS results in Fig. 7. When the fluence is increased to $3.8 \times 10^{15} \text{ cm}^{-2}$, the silicide phases become identifiable. The initially identified silicides are metal-rich in the form of Cr₃Si and FeSi type silicides. As the fluence increases to $>10^{16} \text{ cm}^{-2}$, the silicides change to being more silicon-rich in the form of CrSi₂, CoSi₂, and FeSi₂-type silicides. At a fluence $>10^{16} \text{ cm}^{-2}$, the onset fluence when the fcc phase effectively disappears, the XRD result is consistent with the previous STEM-EDS analysis (Figs. 4 and 9). NiSi, NiSi₂, and CuSi₂ were not included as they align with FeSi and FeSi₂. One phase not identified by fitting the XRD data was the Cu_{0.83}Si_{0.17} phase found in Fig. 9 at a fluence of $2.0 \times 10^{16} \text{ cm}^{-2}$. This could be due to the relatively large depth from the surface and the non-homogeneous nature of this phase throughout the film. Further details about the reference sample and Rietveld analysis are in Supplemental Figs. 4 and 5.

DISCUSSION

Nuclear reactor environments require materials to keep their microstructural stability during simultaneous exposure of materials to extreme radiation and environmental conditions. Multiple principal element alloys generally, and high-entropy alloys specifically, have been cited as possible sets of materials for these extreme environments due to large design space and radiation resistance. However, based on the results here, the microstructural stability of HEAs under multiple extremes clearly depends strongly on the specific environmental exposure during irradiation and on the alloy composition. The CoCrCuFeNi film grown on a layer of SiO₂ remained relatively stable under room temperature ion irradiation up to peak dose of about 500 dpa, while the same film grown on Si began losing stability at the interface with Si at a low dose of about 1 dpa, large-scale phase change started at doses over 6 dpa, and exceptionally large grain size increase by a dose of ~170 dpa. Now that the vast differences between radiation response is clear, it is important to understand the mechanisms for the dramatic changes under room temperature ion irradiation.

It may not be altogether surprising that the irradiation caused large-scale phase instability since each element within the alloy film are known to form silicide phases, and SiO₂ is relatively inert^{38,39}. However, it was not clear that low or room temperature irradiation would cause such instability due to the known low defect generation and mobility/diffusivity in HEAs. Room temperature irradiation reveals the apparent mechanisms for the formation of these silicide phases, with the bases being a combination of ballistic mixing and radiation-enhanced diffusion over short distances at the interface between the film and substrate. Ballistic mixing at the interface may have some impact, but the damage energy imparted at the film–substrate interface (Fig. 3) is about a factor of two difference, but the difference in behavior between the films is much greater than that. Thus, ballistic mixing alone cannot account for the difference between the two films; therefore, the primary origin for the difference between substrates will be shown to be radiation-enhanced diffusion over short distances at the interface between the film and substrate driven by gradients in chemical potential and point defect density. After a fluence of $4.9 \times 10^{13} \text{ cm}^{-2}$, the concentration profile at the film–substrate interface changes slightly relative to the as-grown film (see Fig. 11). The Cu concentration has a small buildup within 3 nm of the interface coupled with a depletion of 3–5 nm from the interface; this depletion region corresponds with an elevation particularly in Co but also in Ni and Fe. This short distance is enough for the radiation-enhanced diffusion of Cu towards the interface with Si despite the low diffusivity in HEAs. The peak of the damage profile (Fig. 3a) at the interface has a much larger damage level than the surrounding film or substrate; thus, there is a large gradient in generated point defects above and below the interface.

These radiation-induced vacancies near the interface preferentially exchange with Cu atoms to move towards the interface, which have a driving force to mix with the Si substrate due to a negative enthalpy of mixing with Si⁴⁰. With increased movement of Cu towards the Si and vacancies moving into the film, in turn the diffusion of the other metal atoms towards the substrate takes place due to the excess vacancy concentration, generally in the order of enthalpies of mixing and atomic radii. This is the same order in which the silicide phases form in the films grown on Si: Cu-, Ni-, Co-, Fe-, and Cr-rich silicides. This is also the order of increasing size of atomic radii and ionic radii for M²⁺ ions except for Cu²⁺ which is slightly larger than Ni²⁺. A similar analysis on oxidation of CoCuFeNiPt HEA nanoparticles highlights the preferential formation of oxides during exposure to oxygen, with Fe having the most stable oxide and thus most readily moves to the surface while the least oxidizing element, Pt, remains in the

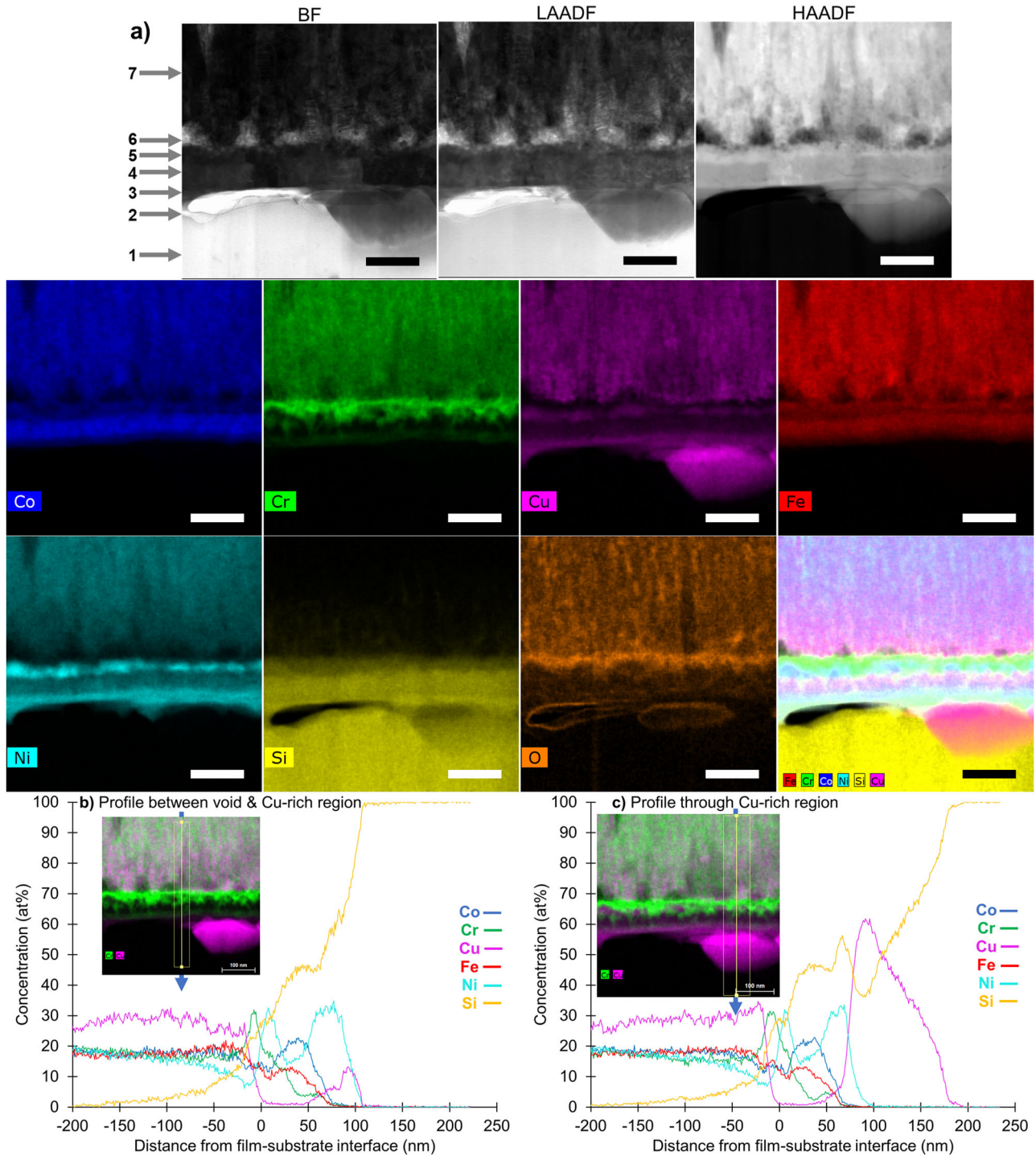


Fig. 7 The interface between the HEA film and Si substrate continues to evolve and form a multilayered structure with a higher Au-ion irradiation dose. a) STEM-BF, LAADF, and HAADF images and EDS maps of the CoCrCuFeNi film grown on a Si substrate after room temperature 11.5 MeV Au-ion irradiation to a fluence of $7.1 \times 10^{14}\text{ cm}^{-2}$ ((peak of ~ 6.1 dpa). Arrows in a highlight the seven regions that are observed. The scale bar length in all images is 100 nm. Concentration profiles normal to the interface b) next to and c) through the Cu-rich region.

core of the nanoparticles⁴¹. The order of preference for formation of oxides in these nanoparticles follows that of the formation energy of the separate oxide. The formation of these multiple silicide phases resembles the formation of various oxide phases during high temperature oxidation of HEA alloys, which are accompanied by substantial oxide scale thicknesses depending on composition¹¹. Similarly, here the metals that most readily form

silicides also form in the same order under room temperature ion irradiation. Low temperature irradiation seemingly is enough to resemble that of high temperature exposure in this system, highlighting the effective driving force of radiation-induced diffusion rather than the thermal-induced diffusion that is based on temperature-dependent vacancy concentration. Further research into very low temperature or cryo-irradiation conditions

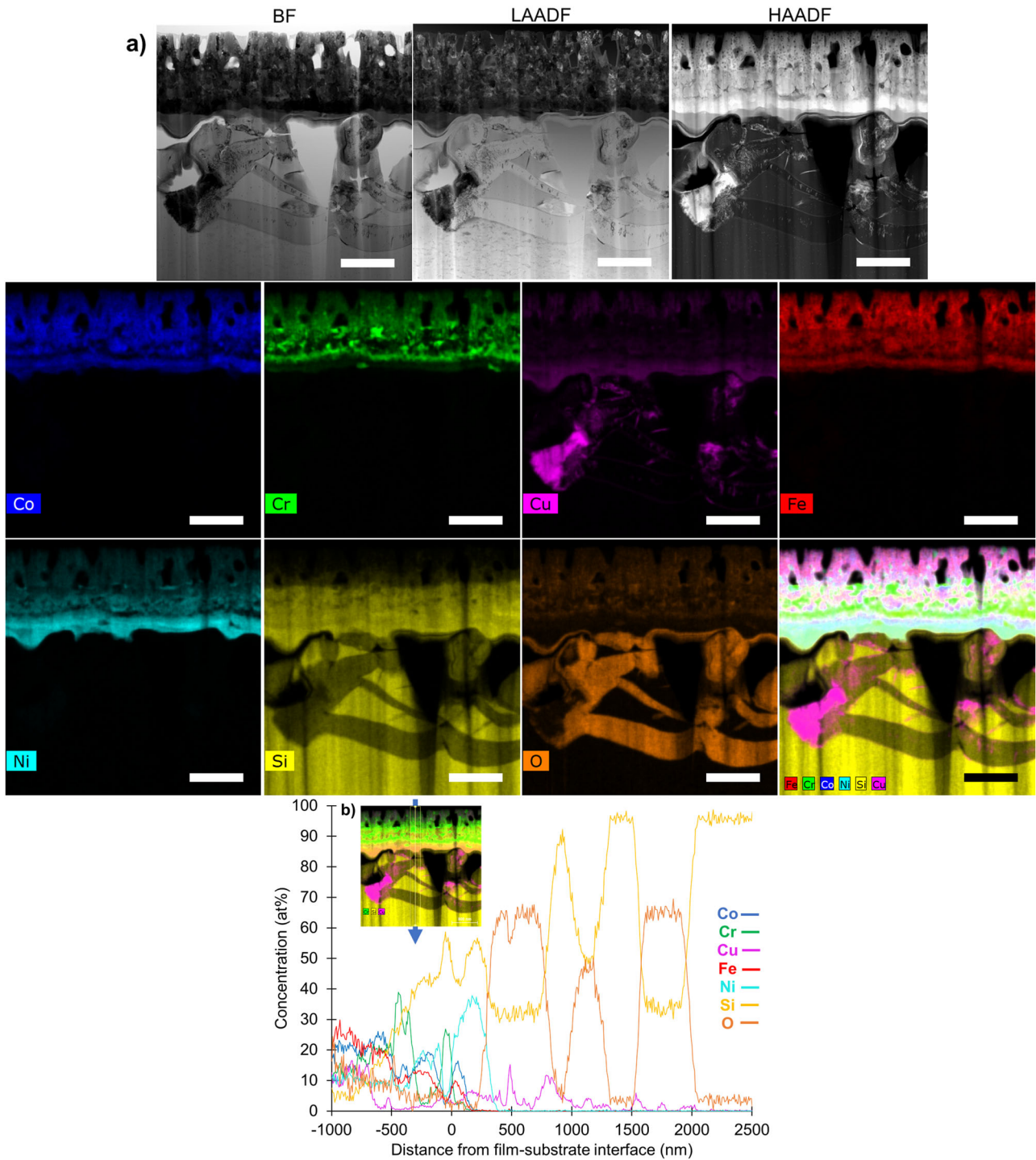


Fig. 8 Large-scale phase has occurred and nearly completely removes the metallic phase at the next highest Au-ion irradiation fluence. **a** STEM-BF, LAADF, and HAADF images and EDS maps of the CoCrCuFeNi film grown on a Si substrate after room temperature 11.5 MeV Au-ion irradiation to a fluence of $3.8 \times 10^{15} \text{ cm}^{-2}$ (peak of ~32.4 dpa). The scale bar length in all images is 800 nm. **b** Concentration profiles normal to the interface.

would be needed to determine if mixing is suppressed below the temperature at which both interstitials and vacancies are immobile.

In addition, Cu, Ni, and Co are known to be the diffusing species in M-Si binary diffusion couples, whereas Si is the diffusing species when Fe and Cr are the metals³⁸. The most rapidly diffusing metallic species move first before Si diffuses upwards to transform the rest

of the film. At the highest fluences of 2.0×10^{16} and $6.0 \times 10^{16} \text{ cm}^{-2}$, Cu-rich silicides are deepest into the substrate, followed by Ni and Co-rich silicides just below the initial film–substrate interface, and Fe and Cr-rich silicides make up the bulk of the silicide at the top, where the initial film was located. In the absence of a strong enthalpic driving force, such as with the insertion of the SiO_2 layer or potentially with the removal of Cu

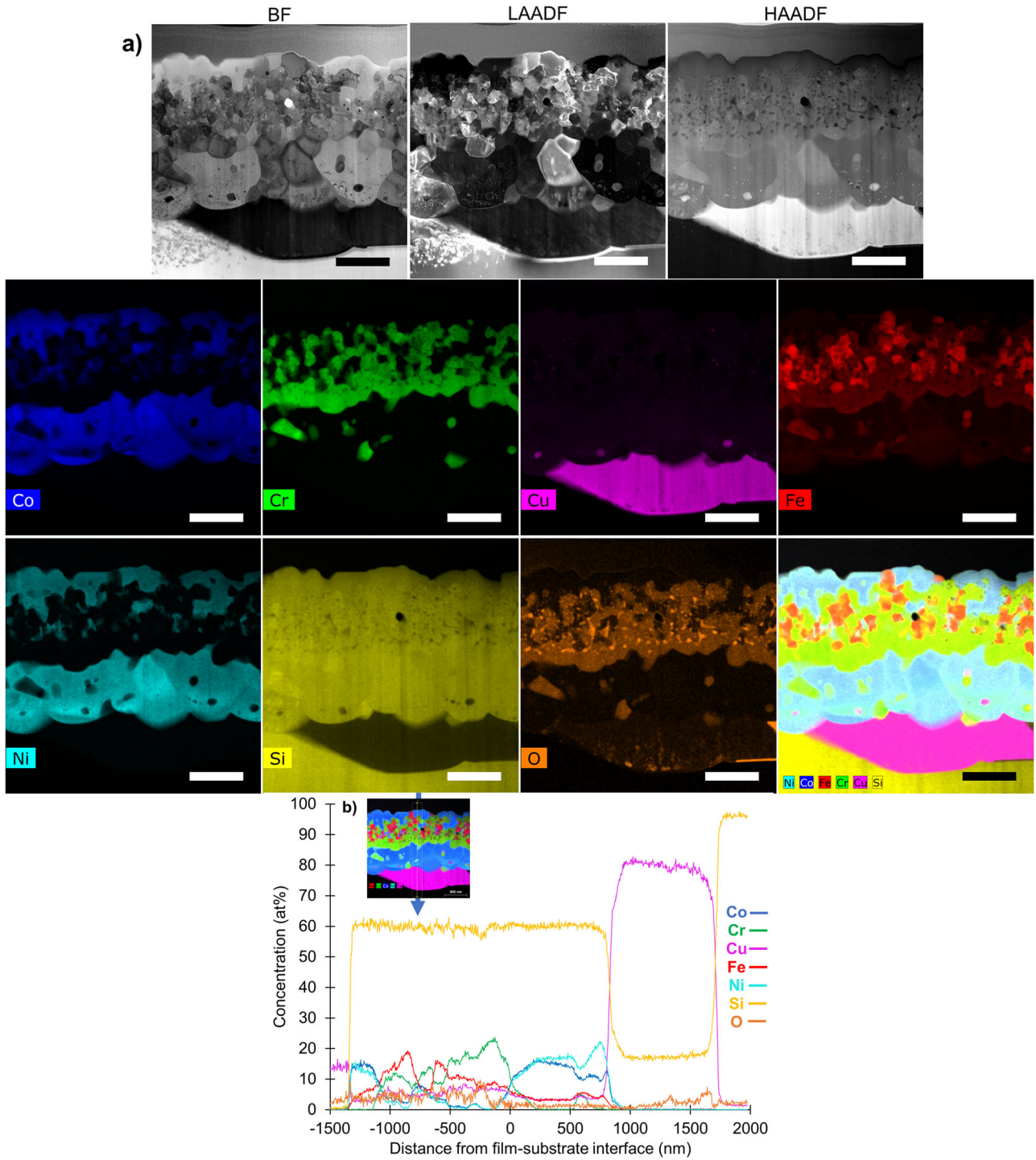


Fig. 9 At the second largest Au-ion irradiation fluence, the HEA film has been completely consumed and multiple thick silicide layers have formed. a STEM-BF, LAADF, and HAADF images and EDS maps of the CoCrCuFeNi film grown on a Si substrate after room temperature 11.5 MeV Au-ion irradiation to a fluence of $2.0 \times 10^{16} \text{ cm}^{-2}$ (peak of $\sim 172.6 \text{ dpa}$). The scale bar length in all images is 800 nm. **b** Concentration profiles normal to the interface.

from the HEA, ballistic mixing alone cannot account for the large degree of phase transformations that take place. Thus, the primary mechanism must be diffusion-based.

This movement of Cu atoms is non-planar, likely aided by grain-boundary diffusion and a net flux of vacancies upwards into the film as Cu preferentially moves downwards at a faster rate than Si moves upwards into the film. The columnar grain width is $\sim 20\text{--}30 \text{ nm}$ initially and grows to about $50\text{--}60 \text{ nm}$ at the fluence

of $7.1 \times 10^{14} \text{ cm}^{-2}$, which is roughly the same size and spacing of the first voids that are observed (Fig. 7). The inverse Kirkendall effect^{42–44}, where there is a net flux of vacancies in the direction opposite of the flux of atoms, is evidenced by the large voids that form above the interface in the film at higher fluences, such as at $7.1 \times 10^{14} \text{ cm}^{-2}$. This is coupled with the substrate being single crystalline, which likely results in some lateral diffusion initially of Cu, but also the other metal atoms, in the film–substrate interface

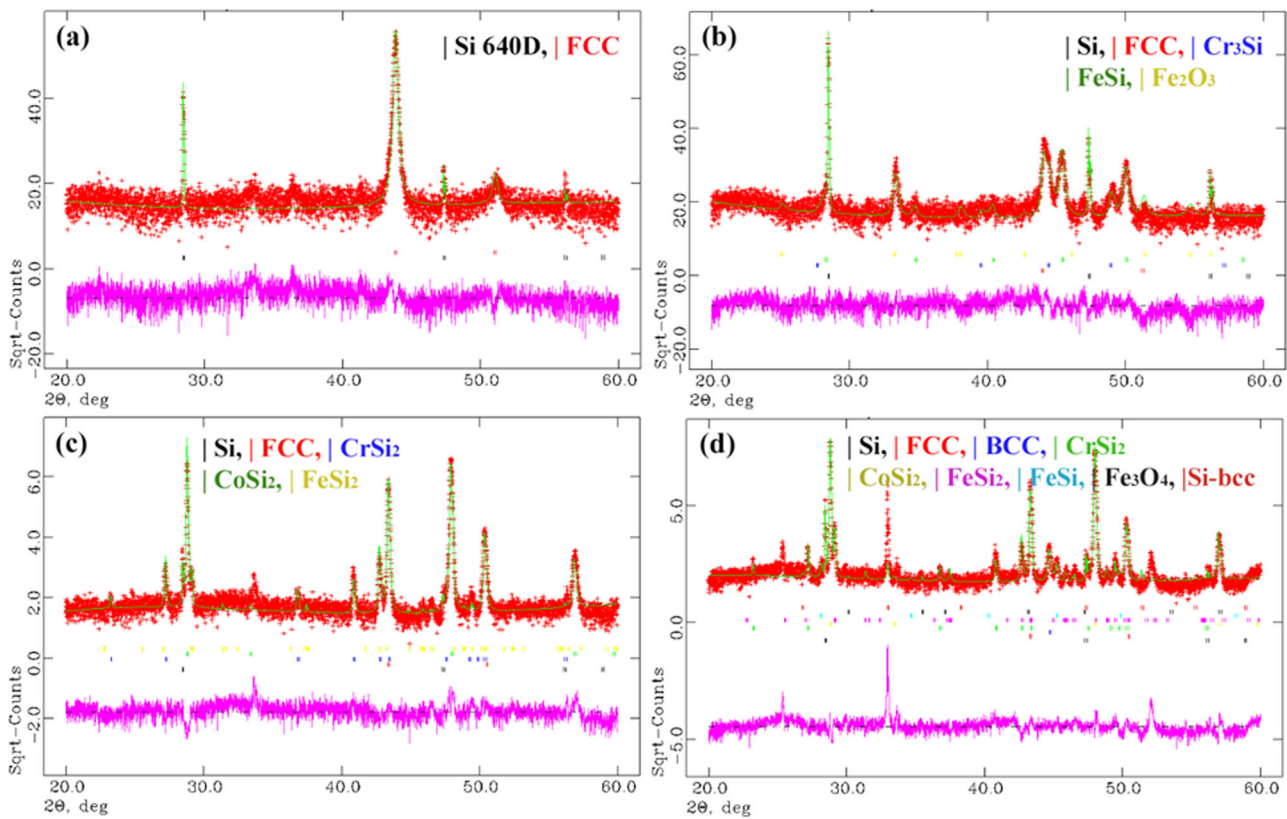


Fig. 10 XRD was used to confirm the phase change behavior as a function of irradiation fluence. XRD profile fits of **a** $7.1 \times 10^{14} \text{ cm}^{-2}$, **b** $3.8 \times 10^{15} \text{ cm}^{-2}$, **c** $2.0 \times 10^{16} \text{ cm}^{-2}$, **d** $6.0 \times 10^{16} \text{ cm}^{-2}$. Only $20\text{--}60^\circ 2\theta$ range is shown for clarity. Color codes of tick marks of different phases are shown on each figure. Pink patterns at bottom of each is the residual between the experimental (red) and the fit (light green) patterns.

Table 3. Quantitative phase compositions (wt%) of the samples irradiated to different fluences.

Phase	4.9×10^{13}	1.2×10^{14}	7.1×10^{14}	3.8×10^{15}	2.0×10^{16}	6.0×10^{16}
FCC	100	100	100	29.3 (3)	8.8 (4)	<2.0
BCC	—	—	—	—	—	9.9 (2)
CrSi ₂	—	—	—	—	37.0 (2)	27.4 (2)
CoSi ₂	—	—	—	—	45.0 (1)	41.9 (1)
FeSi ₂	—	—	—	—	9.2 (3)	15.9 (3)
FeSi	—	—	—	32.7 (3)	—	<3.0
M ₃ O ₄ oxide	—	—	—	—	—	<1.0
M ₂ O ₃ oxide	—	—	—	13.7 (2)	—	—
Cr ₃ Si	—	—	—	24.3 (2)	—	—

Standard deviation of weight fraction is given inside parentheses.

^aA minor peak at 36.4° corresponding to M₃O₄ phases.

the structure after a room temperature irradiation fluence of $3.8 \times 10^{15} \text{ cm}^{-2}$ as seen in Fig. 8. In the case of thermal annealing, the thermal vacancy flux, as opposed to the irradiation-induced vacancy flux, towards the strong defect sink that is the film–substrate interface results in the formation of large voids above the region where Cu and Ni, Co, and Fe have moved into the substrate. Because the driving force is larger for Cu to form a silicide, there are voids even below where the layer of Ni–Co–Fe silicide is found, similarly to the room temperature ion irradiation case.

In addition to the inverse Kirkendall effect in which metallic elements move in the opposite direction of the vacancy flux, there is also a pseudo-solute drag mechanism that simultaneously takes place, though initially at a slower rate, where Si atoms move in the same direction as the vacancy flux⁴⁴. Initially, Cu, Ni, and Co are the primary diffusing atoms, but as the local concentration of these elements near the interface is exhausted and have formed silicides, Si becomes the primary diffusing species as it interacts with more of the film to form Cr and Fe-rich silicides. The mechanism appears to shift from primarily an inverse Kirkendall effect to primarily a solute drag effect. This transition to Si mobility via solute drag is likely enabled by the effectively infinite source of Si while the metallic elements have a relative finite supply. It would be of interest to observe how these interactions would change if the Si substrate were replaced with either a multilayered film composed of HEA and Si layers of varying thicknesses on top of an inert substrate like SiO₂. This could lead to the ability for designing high entropy alloy/high entropy silicide (HEA/HES) composite materials in situ by controlling the source extent of the diffusing species.

plane due to slower bulk matrix diffusion. Also, the void formation likely is enhanced by the reduced rate of diffusion in the HEA film away from the boundary, and thus the vacancies have nowhere to go but to combine into voids just above the film–substrate interface.

The evidence of a radiation-enhanced vacancy diffusion mechanism at room temperature is aided by thermal annealing experiments on the same initial films at elevated temperatures. The behavior of the films after annealing at 500°C for 1.5 h as shown in Fig. 12 (and after 5.5 h of annealing in Supplementary Fig. 3) is nearly the same as the behavior of the films after room temperature. After 1.5 h of annealing, the film strongly resembles

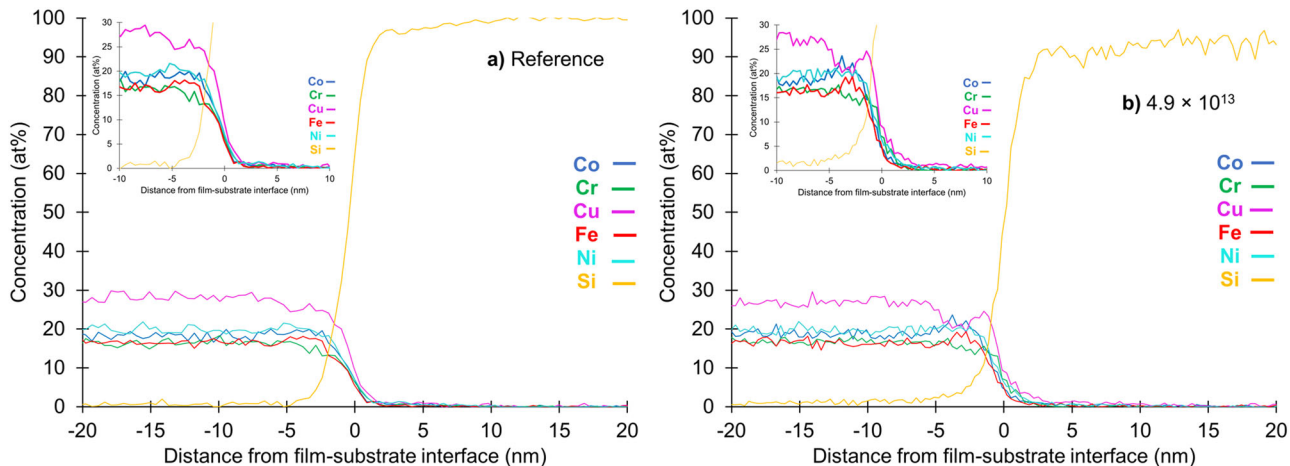


Fig. 11 Concentration profiles across the film–substrate interface highlight the initial compositional fluctuation after very low fluence Au-ion irradiation. STEM-EDS concentration profiles normal to the interface of the **a** as-grown film and the **b** film irradiated to a fluence of $4.9 \times 10^{13} \text{ cm}^{-2}$.

As the metallic film is consumed and transformed into silicide phases, the restructuring of the film from columnar grains to large, more equiaxed grains takes place. For the film grown on Si, the degree of grain growth is remarkable, as increasing the dose by a factor of ~ 500 (from the as-grown film or a low fluence condition of $1.1 \times 10^{14} \text{ cm}^{-2}$ up to the highest fluence of $6.0 \times 10^{16} \text{ cm}^{-2}$) increases the grain size by a factor of 8–13. The large-scale grain growth seems to have only occurred once the film transformed into a multiple silicide phase, as the film grown on SiO_2 up to the same high dose had columnar widths grow by a factor of < 1.5 . Thus, the substantial grain growth is a ceramic or insulator-based phenomenon, likely partially due to localized heating as a result of electronic energy deposition through inelastic thermal spikes throughout the thickness of the film that is unable to be dissipated due to the poor conductivity^{37,45}. Varying the ion energy, the ion mass, and radiation dose rate likely would have an influence on the kinetics of this grain growth and the phase transformations and could provide details as to the effects of electronic energy deposition through inelastic thermal spikes compared to damage energy deposition through elastic thermal spikes³⁷. However, the very high degree of grain growth at room temperature likely also needs another mechanism, such as a high degree of localized strain or high interface energy. The cause of this large grain growth is somewhat speculative and would be of interest for further study.

In summary, two sets of near-equiatomic CoCrCuFeNi HEA thin films were irradiated at room temperature with 11.5 MeV Au ions: one set was grown on a single crystal Si substrate and the other set was grown on a single crystal Si substrate with a 100 nm thick SiO_2 on top of it. The behavior of each set of films was drastically different and was comparable to how these materials would behave under exposure to corrosion or inert environments. The film grown on SiO_2 had relatively minimal change with some small degree of compositional fluctuation, a small degree of grain growth, and no interaction with the substrate up to doses with peak damage levels above 500 dpa. The film grown on Si underwent changes at the substrate-film interface at peak doses as low as 0.1 dpa and completely transformed into a multi-silicide film at peak doses above 32 dpa followed by substantial grain growth up the highest dose of over 500 dpa. The large changes are remarkable given that this irradiation is done at room temperature where thermally induced growth is minimized.

Similar to the formation of oxide scales during high temperature exposure of similar HEAs to air or water, the silicides form in the same order as which the metals' atomic radii and silicide formation energy. The primary mechanism is radiation-enhanced

diffusion by means of the inverse Kirkendall effect and the solute drag effect. Similar thermal-based behaviors are only found after high temperature annealing. The results presented here highlight the effect of environmental/surrounding condition (e.g., Si vs. SiO_2) has on the behavior of HEAs under radiation. The initial diffusion of Cu into the Si substrate suggests composition of the HEA film has a profound effect on phase stability, but more research is needed to understand how changing the composition relative to the equiatomic composition affects the behavior under synergistic exposure and radiation, and how other HEA classes perform beyond the single-phase fcc alloys presented here. The results also highlight that controlling the diffusion rates via the extent of elemental sources could be used to produce unique composite materials during in-situ exposure under irradiation.

METHODS

High entropy alloy thin film growth, heavy ion irradiation, and annealing

Nanocrystalline films of near-equiatomic CoCrCuFeNi high entropy alloys were sputter deposited on Si(100) wafers and $\text{SiO}_2/\text{Si}(100)$ wafers, which have a 100 nm-thick SiO_2 surface layer on top of the Si substrate. As confirmed by cross-sectional transmission electron microscopy (TEM) and XRD, the film thickness was grown to ~ 1000 nm. The film was sputter deposited, consuming a 50 mm diameter equiatomic composition target using 200 W DC sputtering. During the sputtering, no intentional substrate heating was applied.

Heavy ion irradiation was conducted at the Ion Beam Materials Laboratory at the University of Tennessee-Knoxville⁴⁶ using 11.5 MeV Au ions to various fluences from 4.9×10^{13} up to $6.0 \times 10^{16} \text{ cm}^{-2}$ at a flux of $3.3 \times 10^{12} \text{ cm}^{-2} \text{ s}^{-1}$ at room temperature in ultra-high vacuum to evaluate the microstructural changes of these fcc nanostructured HEAs and their response in various environments—based on substrate difference. Heating from the ion beam was minimal with a maximum temperature rise of about 50 °C⁴⁷. To ensure a uniform irradiation, the ion beam was defocused and wobbled over the sample surface during the irradiation with horizontal and vertical scan frequency of 517 and 64 Hz, respectively.

Annealing was also carried out to help determine mechanisms for elemental mobility during room temperature irradiation. Separate films that were not irradiated were also annealed at 500 °C in the same ultra high vacuum conditions for 1.5 and 5.5 h, the latter of which is the approximate time of the longest duration irradiation treatment.

Characterization by scanning transmission electron microscopy

Microstructural characterization via focused ion beam (FIB)/scanning electron microscopy (SEM), TEM, and STEM was used to analyze the microstructural and microchemical evolution of the HEA film after

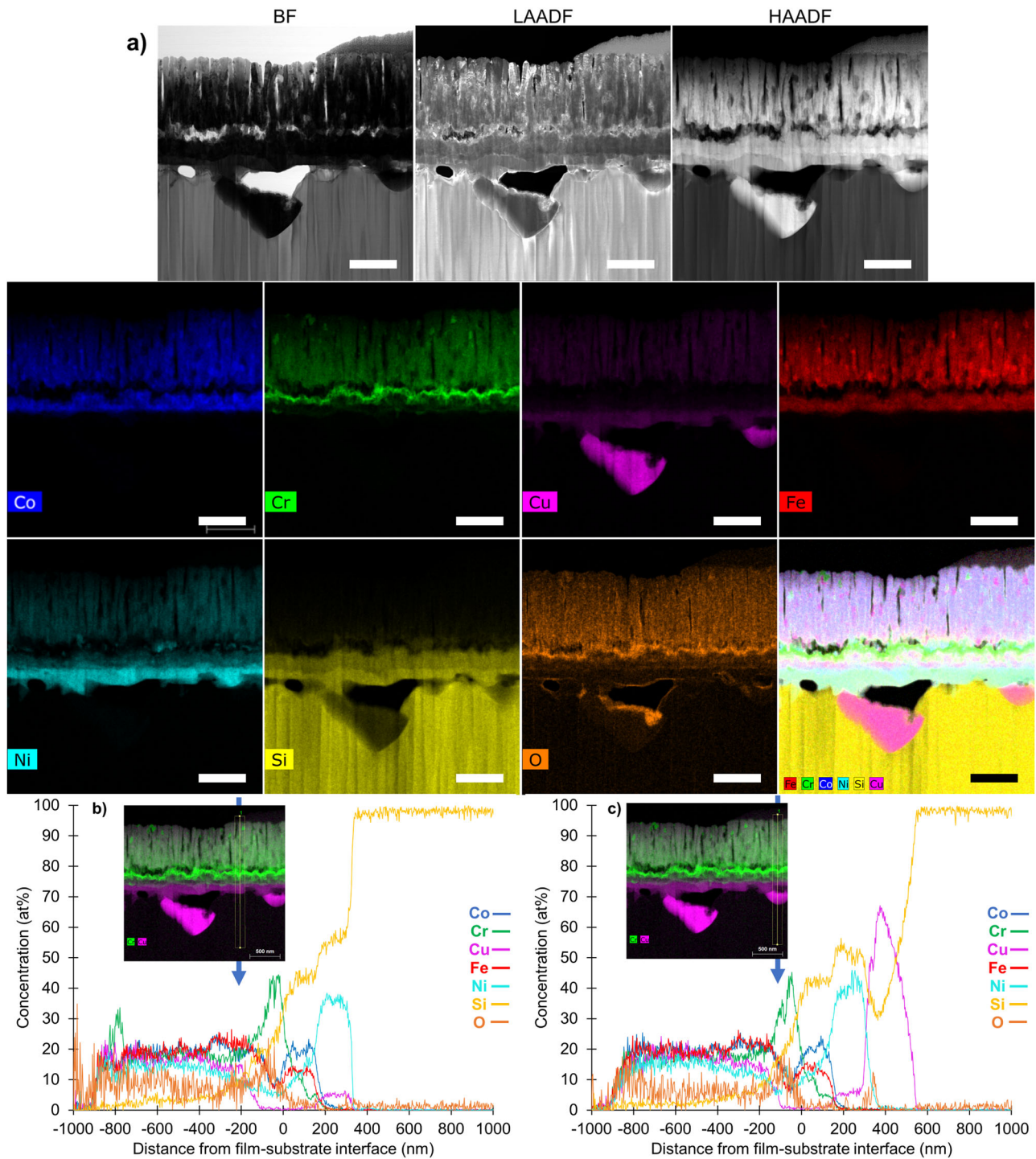


Fig. 12 High temperature annealing results in similar behavior as room-temperature ion irradiation. **a**, STEM-BF, LAADF, and HAADF images and **c**, EDS maps of the CoCrCuFeNi film grown on a Si substrate after annealing at 500 °C for 1.5 h in an ultra-high vacuum chamber. The scale bar length in all images is 500 nm. **b**, **c**, Concentration profiles normal to the interface at different locations.

irradiation or annealing. FIB/SEM was conducted on a FEI Versa 3D FIB to make electron-transparent TEM lamellae by using standard lift-out and thinning techniques. The lamellae were lifted out by using 16 kV Ga ions and thinning to electron transparency was performed by using 8 and 5 kV Ga ions followed by fine polishing at 2 kV. The lamellae were then transferred to a Fischione Model 1040 Nanomill, where damage from the FIB was removed by using 900 eV Ar ions. TEM bright-field (BF) and through-focus imaging, along with STEM-BF and STEM-annular DF (ADF) imaging were used to visualize microstructural evolution. TEM and STEM

imaging were conducted on these specimens by using a Thermo Fisher (formerly FEI) Talos F200X 200 keV STEM equipped with an X/field emission gun (FEG) high-brightness emission source, BF and multiple ADF detectors at different collection angles denoted as low angle ADF (LAADF), medium angle ADF (MAADF), and high angle ADF (HAADF), and a quadrupole FEI SuperX EDS collection system. The collection angles at a 98 mm camera length for each ADF detector are 12–20 mrad for LAADF, 24–57 mrad for MAADF, and 61–200 mrad for HAADF. The EDS system allowed for detailed analysis of the microstructural and

microchemical evolution in the multi-element near-equiautomic alloys after irradiation or annealing.

Characterization by X-ray powder diffraction

A D2 Phaser, Bruker Inc., Benchtop X-ray diffractometer with a maximum operating tube power of 0.3 kW (30 kV and 10 mA) and Cu K α radiation was used in this study. All the XRD patterns were collected using a 0.004 step size and in a 10–110° 2 θ range over ~10 h acquisition time. A NIST Si-SRM640D internal standard was used to correct any sample displacement error. Phase identification of the samples based on the Bragg reflections in their XRD patterns was performed using Panalytical HighScorePlus software (Malvern Panalytical B.V. Almelo, the Netherlands) equipped with ICDD PDF-4+ crystallography database. Rietveld analysis was used to fit the experimental XRD patterns using GSAS software^{48,49}. Backgrounds of some XRD patterns were first corrected using OriginPro software to get rid of any anomalies during peak fitting.

DATA AVAILABILITY

The datasets generated during and/or analyzed during the current study are available from the corresponding author on reasonable request.

Received: 16 February 2022; Accepted: 26 May 2022;

Published online: 20 July 2022

REFERENCES

- Schmidt, F. et al. Effects of radiation-induced defects on corrosion. *Annu. Rev. Mater. Res.* **51**, 293–328 (2021).
- Zhang, X. et al. Radiation damage in nanostructured materials. *Prog. Mater. Sci.* **96**, 217–321 (2018).
- El-Atwani, O. et al. Outstanding radiation resistance of tungsten-based high-entropy alloys. *Sci. Adv.* **5**, eaav2002 (2019).
- Wang, X., Guo, W. & Fu, Y. High-entropy alloys: emerging materials for advanced functional applications. *J. Mater. Chem. A* **9**, 663–701 (2021).
- Osetsky, Y. et al. Tunable chemical complexity to control atomic diffusion in alloys. *npj Comput. Mater.* **6**, 38 (2020).
- Zhang, Y. et al. Thermal stability and irradiation response of nanocrystalline CoCrFeNi high-entropy alloy. *Nanotechnology* **30**, 294004 (2019).
- Lu, C. et al. Enhancing radiation tolerance by controlling defect mobility and migration pathways in multicomponent single-phase alloys. *Nat. Commun.* **7**, 13564 (2016).
- Pickering, E. J. et al. High-entropy alloys for advanced nuclear applications. *Entropy* **23**, 98 (2021).
- Zhang, Y., Osetsky, Y. N. & Weber, W. J. Tunable chemical disorder in concentrated alloys: defect physics and radiation performance. *Chem. Rev.* **122**, 789–829 (2022).
- Zhang, Z., Armstrong, D. E. J. & Grant, P. S. The effects of irradiation on CrMnFeCoNi high-entropy alloy and its derivatives. *Prog. Mater. Sci.* **123**, 100807 (2022).
- Kai, W. et al. Air-oxidation of FeCoNiCr-based quinary high-entropy alloys at 700–900 °C. *Corros. Sci.* **121**, 116–125 (2017).
- Shi, H. et al. Oxidation behavior and microstructure evolution of alumina-forming austenitic & high entropy alloys in steam environment at 1200 °C. *Corros. Sci.* **170**, 108654 (2020).
- Osei-Agyemang, E. & Balasubramanian, G. Surface oxidation mechanism of a refractory high-entropy alloy. *npj Mater. Degrad.* **3**, 20 (2019).
- Wang, P. & Was, G. S. Oxidation of Zircaloy-4 during in situ proton irradiation and corrosion in PWR primary water. *J. Mater. Res.* **30**, 1335–1348 (2015).
- Lillard, R. S., Paciotti, M. & Tchernotskaia, V. The influence of proton irradiation on the corrosion of HT-9 during immersion in lead bismuth eutectic. *J. Nucl. Mater.* **335**, 487–492 (2004).
- Frazer, D. et al. Degradation of HT9 under simultaneous ion beam irradiation and liquid metal corrosion. *J. Nucl. Mater.* **479**, 382–389 (2016).
- Zhou, W. et al. Proton irradiation-decelerated intergranular corrosion of Ni-Cr alloys in molten salt. *Nat. Commun.* **11**, 3430 (2020).
- Chen, W.-Y. et al. Irradiation effects in high entropy alloys and 316H stainless steel at 300 °C. *J. Nucl. Mater.* **510**, 421–430 (2018).
- Xu, Q., Guan, H. Q., Zhong, Z. H., Huang, S. S. & Zhao, J. J. Irradiation resistance mechanism of the CoCrFeMnNi equiautomic high-entropy alloy. *Sci. Rep.* **11**, 608 (2021).
- Li, C. et al. Neutron irradiation response of a Co-free high entropy alloy. *J. Nucl. Mater.* **527**, 151838 (2019).
- Schreiber, D. K. et al. Revealing the complexity of high temperature oxide formation in a 38Ni–21Cr–20Fe–13Ru–6Mo–2W (at. %) multi-principal element alloy. *Scr. Mater.* **210**, 114419 (2022).
- Quiambaro, K. F. et al. Passivation of a corrosion resistant high entropy alloy in non-oxidizing sulfate solutions. *Acta Mater.* **164**, 362–376 (2019).
- Scully, J. R. et al. Controlling the corrosion resistance of multi-principal element alloys. *Scr. Mater.* **188**, 96–101 (2020).
- Kautz, E. J. et al. Element redistributions during early stages of oxidation in a Ni38Cr22Fe20Mn10Co10 multi-principal element alloy. *Scr. Mater.* **194**, 113609 (2021).
- Qiu, Y., Gibson, M. A., Fraser, H. L. & Birbilis, N. Corrosion characteristics of high entropy alloys. *Mater. Sci. Technol.* **31**, 1235–1243 (2015).
- Peng, X. & Chen, L. Effect of high entropy alloys TiCrZrHf barrier layer on microstructure and texture of Cu thin films. *Mater. Lett.* **230**, 5–8 (2018).
- Kumar, A., Kumar, M. & Kumar, D. Effect of composition on electroless deposited Ni–Co–P alloy thin films as a diffusion barrier for copper metallization. *Appl. Surf. Sci.* **258**, 7962–7967 (2012).
- Chang, S.-Y., Wang, C.-Y., Chen, M.-K. & Li, C.-E. Ru incorporation on marked enhancement of diffusion resistance of multi-component alloy barrier layers. *J. Alloy. Compd.* **509**, L85–L89 (2011).
- Tsai, M.-H. et al. Thermal stability and performance of NbSiTaTiZr high-entropy alloy barrier for copper metallization. *J. Electrochem. Soc.* **158**, H1161 (2011).
- Weber, W. J. & Zhang, Y. Predicting damage production in monoatomic and multi-elemental targets using stopping and range of ions in matter code: challenges and recommendations. *Curr. Opin. Solid State Mater. Sci.* **23**, 100757 (2019).
- Zhang, Y. & Weber, W. J. Ion irradiation and modification: the role of coupled electronic and nuclear energy dissipation and subsequent nonequilibrium processes in materials. *Appl. Phys. Rev.* **7**, 41307 (2020).
- Zhang, L., Du, Y., Xu, H. & Pan, Z. Experimental investigation and thermodynamic description of the Co–Si system. *Calphad* **30**, 470–481 (2006).
- Du, Y. & Schuster, J. C. Experimental reinvestigation of the CrSi–Si partial system and update of the thermodynamic description of the entire Cr–Si system. *J. Phase Equilib.* **21**, 281–286 (2000).
- Okamoto, H. Cu–Si (copper–silicon). *J. Phase Equilib.* **23**, 281 (2002).
- Lindholm, M. A thermodynamic description of the Fe–Cr–Si system with emphasis on the equilibria of the sigma (Σ) phase. *J. Phase Equilib.* **18**, 432 (1997).
- Miettinen, J. Thermodynamic description of the Cu–Ni–Si system in the copper-rich corner above 700 °C. *Calphad* **29**, 212–221 (2005).
- Zhang, Y. et al. Role of electronic energy loss on defect production and interface stability: comparison between ceramic materials and high-entropy alloys. *Curr. Opin. Solid State Mater. Sci.* **26**, 101001 (2022).
- Zhang, L. *A Kinetic Model For Silicide Formation Through Solid State Reactions in Metal-silicon Diffusion Couples*. ProQuest Dissertations and Theses. University of Alberta, Canada (1993).
- Cahoon, E. C., Comrie, C. M. & Pretorius, R. The reaction between thin Ni and Co films and their disilicides. *MRS Proc.* **25**, 57 (1983).
- Shin, D., Saal, J. E. & Liu, Z.-K. Thermodynamic modeling of the Cu–Si system. *Calphad* **32**, 520–526 (2008).
- Song, B. et al. In situ oxidation studies of high-entropy alloy nanoparticles. *ACS Nano* **14**, 15131–15143 (2020).
- Marwick, A. D. Segregation in irradiated alloys: the inverse Kirkendall effect and the effect of constitution on void swelling. *J. Phys. F* **8**, 1849–1861 (1978).
- Chen, W.-Y., Poplawsky, J. D., Chen, Y., Guo, W. & Yeh, J.-W. Irradiation-induced segregation at dislocation loops in CoCrFeMnNi high entropy alloy. *Materialia* **14**, 100951 (2020).
- Ardell, A. J. & Bellon, P. Radiation-induced solute segregation in metallic alloys. *Curr. Opin. Solid State Mater. Sci.* **20**, 115–139 (2016).
- Zhang, Y. et al. The effect of electronic energy loss on irradiation-induced grain growth in nanocrystalline oxides. *Phys. Chem. Chem. Phys.* **16**, 8051–8059 (2014).
- Zhang, Y. et al. New ion beam materials laboratory for materials modification and irradiation effects research. *Nucl. Instrum. Methods Phys. Res. Sect. B* **338**, 19–30 (2014).
- Crespillo, M. L., Graham, J. T., Zhang, Y. & Weber, W. J. Temperature measurements during high flux ion beam irradiations. *Rev. Sci. Instrum.* **87**, 24902 (2016).
- Larson, A. C. & Von Dreele, R. B. *General Structure Analysis System (GSAS)*. Los Alamos National Laboratory Report LAUR 86-748 (Los Alamos National Laboratory, 2004).
- Silva, C. M., Rosseel, T. M. & Holliday, K. S. Radiation-induced changes in single crystal calcite and dolomite: mineral analogues of light water reactor, nuclear power plant concrete aggregates. *J. Phys. Chem. C* **126**, 634–646 (2022).

ACKNOWLEDGEMENTS

This work was supported as part of Energy Dissipation to Defect Evolution (EDDE), an Energy Frontier Research Center funded by the U.S. Department of Energy, Office of Science, Basic Energy Sciences, under contract number DE-AC05-00OR22725. This work was also supported in part by Fusion Materials program through the U.S. Department of Energy, Office of Science, Fusion Energy Sciences. The ion irradiations were performed at the Ion Beam Materials Laboratory located at the University of Tennessee, Knoxville. P.D.R. acknowledges support from the Center for Nanophase Materials Sciences from the U.S. Department of Energy (DOE) under grant No# KC0403040 ERKCZ01. This work was also partly performed under the auspices of the U.S. Department of Energy by Lawrence Livermore National Laboratory (LLNL) under Contract No. DE-AC52-07NA27344. This manuscript has been authored by UT-Battelle, LLC under Contract No. DE-AC05-00OR22725 with the US Department of Energy (DOE). The US government retains and the publisher, by accepting the article for publication, acknowledges that the US government retains a nonexclusive, paid-up, irrevocable, worldwide license to publish or reproduce the published form of this manuscript, or allow others to do so, for US Government purposes. DOE will provide public access to these results of federally sponsored research in accordance with the DOE Public Access Plan (<http://energy.gov/downloads/doe-public-access-plan>).

AUTHOR CONTRIBUTIONS

T.G.L.: Formal analysis, investigation, methodology, visualization, writing—original draft, writing—review and editing; C.M.S.: Data curation, formal analysis, methodology, writing—review and editing; Y.Z.: Methodology, writing—review and editing; W.L.B.: Methodology, writing—review and editing; P.D.R.: Methodology, writing—review and editing; W.J.W.: Conceptualization, methodology, writing—review and editing; Y.Z.: Conceptualization, project administration, supervision, funding acquisition, writing—review and editing.

COMPETING INTERESTS

The authors declare no competing interests.

ADDITIONAL INFORMATION

Supplementary information The online version contains supplementary material available at <https://doi.org/10.1038/s41529-022-00260-2>.

Correspondence and requests for materials should be addressed to Timothy G. Lach.

Reprints and permission information is available at <http://www.nature.com/reprints>

Publisher's note Springer Nature remains neutral with regard to jurisdictional claims in published maps and institutional affiliations.



Open Access This article is licensed under a Creative Commons Attribution 4.0 International License, which permits use, sharing, adaptation, distribution and reproduction in any medium or format, as long as you give appropriate credit to the original author(s) and the source, provide a link to the Creative Commons license, and indicate if changes were made. The images or other third party material in this article are included in the article's Creative Commons license, unless indicated otherwise in a credit line to the material. If material is not included in the article's Creative Commons license and your intended use is not permitted by statutory regulation or exceeds the permitted use, you will need to obtain permission directly from the copyright holder. To view a copy of this license, visit <http://creativecommons.org/licenses/by/4.0/>.

© UT-Battelle, LLC 2022